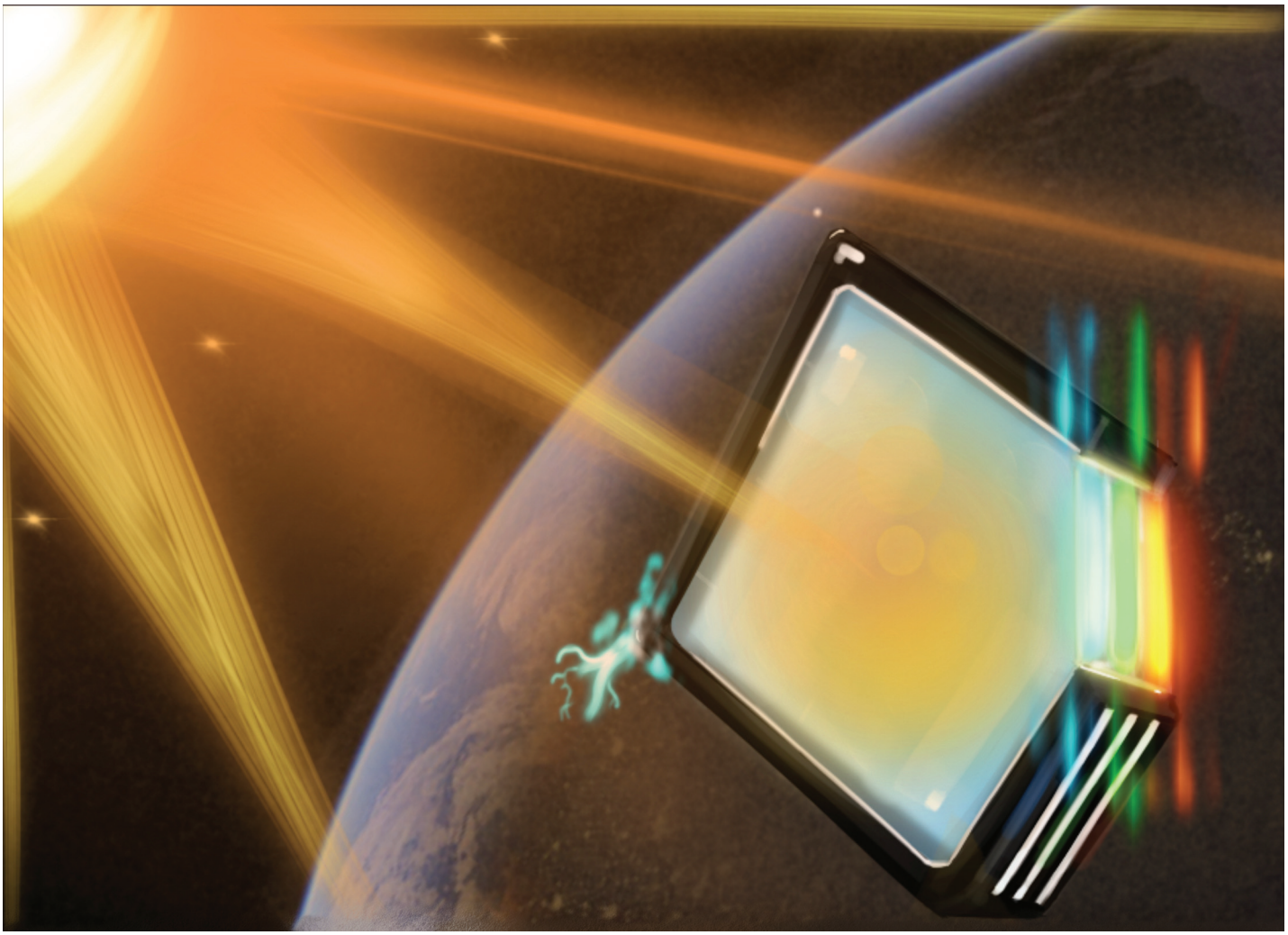

Showcasing Research from the Regional Centre of Advanced Technologies and Materials (RCPTM), Palacky University Olomouc, Faculty of Science.

A carbon dot-based tandem luminescent solar concentrator

Luminescent solar concentrators (LSCs) have been gaining interest in solar light harvesting. However, the use of expensive and unsafe materials has hindered the widespread adoption of such devices. A tandem LSC based exclusively on carbon dots operating in the almost whole range of visible spectra, and showing internal optical quantum efficiency of 23.6% and external optical quantum efficiency of 2.3% is demonstrated.

As featured in:

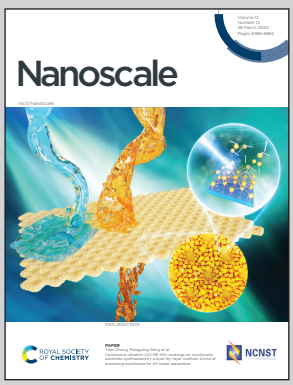

See Radek Zbořil *et al.*, *Nanoscale*, 2020, **12**, 6664.

ROYAL SOCIETY OF CHEMISTRY

rsc.li/nanoscale

Registered charity number: 207890

Nanoscale

PAPER

Cite this: *Nanoscale*, 2020, **12**, 6664

A carbon dot-based tandem luminescent solar concentrator†

Lukáš Zdražil, [a] Sergii Kalytchuk, [a] Kateřina Holá,[a] Martin Petr,[b] Oldřich Zmeškal,[c] Štěpán Kment,[a] Andrey L. Rogach [a,d] and Radek Zbořil *[a]

Received 25th November 2019,
Accepted 24th January 2020

DOI: 10.1039/c9nr10029f

rsc.li/nanoscale

Luminescent solar concentrators (LSCs) are light-management devices and are used for harvesting and concentrating solar light from a large area to their edges. Being semitransparent devices, LSCs show great promise for future utilization in glass walls of urban buildings as environmentally friendly photovoltaic power plants. The development of cheap and eco-safe materials, the extension of the LSC operation range, and the enhancement of the optical efficiency are the key challenges, which need to be solved in order to transform energetically passive buildings into self-sustainable units. Herein, a large area (64 cm^2) tandem LSC fabricated using entirely eco-friendly highly emissive blue, green, and red carbon dots is demonstrated, with an internal optical quantum efficiency of 23.6% and an external optical quantum efficiency of 2.3%, while maintaining a high transparency across the visible spectrum. This opens up a new direction for the application of carbon dots in advanced solar light harvesting technologies.

Introduction

Luminescent solar concentrators (LSCs) are sunlight collectors containing highly emissive fluorophores embedded in or coated onto the top of a transparent material (such as glass or plastic), and are able to concentrate solar light from large surface areas to their edges. Photons absorbed by luminophores from the LSC surface are reemitted at longer wavelengths, redirected by the total internal reflection to the edges, and afterward collected and converted into electrical energy by solar cells attached along the LSC perimeter.[1] Due to the reasonably higher efficiency and lower cost of LSCs than those of a solar cell of the same size, their use can significantly reduce the cost of solar electricity. The integration of semitransparent LSCs into glass walls of urban buildings could transform currently passive facades into self-powered units. However, the wide use of LSCs is still limited by a lack of suitable, eco-friendly, and cost-efficient luminescent materials.

The main parameter for evaluating the performance of LSCs is their optical quantum efficiency (OQE), which is defined as the ratio of the number of photons emitted from the LSC edges to the total number of absorbed photons.[2] Since a large part of converted photons is lost due to reabsorption processes, designing the bandgap structure of emitters to achieve a large Stoke's shift is one of the strategies to achieve high OQE of LSCs.[2–6] Combining this with a high photoluminescence quantum yield (PL QY) led to the fabrication of large 100 cm^2 LSC panels based on traditional semiconductor quantum dots[3,4] or perovskite nanoplatelets[2] with internal OQE of over 20%. Another option to enhance the performance of LSCs is to increase the number of photons which can be absorbed by the device. At the same time, high transparency of the final device is required to realize semitransparent urban photovoltaic power plants.[7] Engineering a tandem LSC structure, in which different types of fluorophores embedded in each separate layer of the LSC are designed to absorb a different part of the solar spectrum, offers an alternative approach to tackle the abovementioned issue.[8]

Different types of fluorophores have been explored in the context of LSC applications such as molecular organic fluorophores,[9,10] fluorescent proteins,[11] perovskite nanocrystals,[2,12–14] and semiconductor quantum dots,[4–6,8,15–20] including heavy-metal-free quantum dots,[3,21,22] semiconductor quantum wells,[23] and nanorods.[24] In recent years, a new class of luminescent nanoparticles termed carbon dots (CDs) have been considered to be suitable candidates for embedding in LSCs.[25–31] An attractive feature of CDs is

[a]*Regional Centre of Advanced Technologies and Materials, Department of Physical Chemistry, Palacký University Olomouc, Šlechtitelů 27, 783 71 Olomouc, Czech Republic. E-mail: radek.zboril@upol.cz*
[b]*Regional Centre of Advanced Technologies and Materials, Department of Experimental Physics, Palacký University Olomouc, Šlechtitelů 27, 783 71 Olomouc, Czech Republic*
[c]*Faculty of Chemistry, Brno University of Technology, Purkyňova 118, 612 00 Brno, Czech Republic*
[d]*Department of Materials Science and Engineering, and Centre for Functional Photonics (CFP), City University of Hong Kong, 83 Tat Chee Avenue, Kowloon, Hong Kong S.A.R*

†Electronic supplementary information (ESI) available. See DOI: 10.1039/c9nr10029f

that they do not contain heavy metals and can be synthesized on a large scale *via* cheap and "green" synthesis protocols.[32] Furthermore, their tunable emission spectra, high photostability, and large molar absorption coefficient are well suited for capturing solar radiation. CDs have already found applications in biomedicine,[33–36] photovoltaics,[37] LEDs,[38] anti-counterfeiting,[39] and lasing,[40] and thus can be considered as an alternative to other types of fluorophores for utilization in LSCs. Several single-layer LSC devices based on CDs have been demonstrated in the literature, but they still suffer from the limited spectral coverage of the solar spectrum, working mainly in the UV-blue range.[25–31] This limitation can be overcome by designing a tandem LSC with several different emitters, each operating in a specific spectral range. Several attempts to realize tandem LSCs exploiting CDs[26] and combinations of CDs with perovskite nanocrystals,[41] molecules with aggregation-induced emission,[42] or organic dyes[43] were made. To the best of our knowledge, three-layered tandem LSCs based exclusively on CDs have not been realized yet.

In this work, we report the fabrication of a highly efficient large area (64 cm^2) tandem LSC consisting of blue-, green-, and red-emitting CD-based sub-LSCs capable of absorbing 9.6% of solar photons. This tandem LSC reaches an internal OQE of 23.6%, and an external OQE of 2.3% both of which show a significant enhancement compared with those of previously reported large-scale CD-based LSCs[26,31] and are comparable with the latest results reported for hybrid tandem structures.[41,42] The fabricated CD-based LSC exhibits high transparency (an average transmittance of 83.4% in the visible range, as calculated from the transmittance spectra presented in Fig. S1†), and the fabrication process of the device, including all its constituting components, is cheap and environmentally friendly. Therefore, the CD-based tandem LSC reported herein provides a promising alternative to classical semiconductor and perovskite quantum dot LSCs.

Experimental

Reagents and materials

Anhydrous citric acid (≥99.5%), L-cysteine (≥97%), perylene (≥99%), sodium hydroxide (≥98%), polyvinyl alcohol ($M_w \approx$ 27 000), polyvinylpyrrolidone ($M_w \approx$ 40 000) and polyvinylpyrrolidone K 30 ($M_w \approx$ 40 000), silica gel (pore size 60 Å), and branched polyethylenimine ($M_w \approx$ 25 000) were purchased from Sigma-Aldrich, and ethyl alcohol (96%), methanol G.R., and nitric acid (65% G.R.) were purchased from Lach-Ner. All chemicals were used directly without any further purification. Milli-Q water (Merck Millipore) was used as a solvent.

Synthesis of b-CDs, g-CDs, and r-CDs

Blue, green, and red emissive CDs were prepared *via* a hydrothermal or solvothermal method following previously published protocols.[44,45]

b-CDs. 1.83 g of citric acid (CA) monohydrate was mixed with 1 g of L-cysteine and the mixture was dissolved in 5 mL of ultrapure water and heated at 70 °C for 12 h to form a thick syrup. The syrup was transferred to a Teflon-lined stainless-steel autoclave (Parr Instrument Company) to undergo hydrothermal treatment at 200 °C for 3 h. The resulting dark acidic syrup was collected and neutralized with 1 M NaOH solution, dissolved in 20 mL of water, and then centrifuged at 6000 rpm to remove the precipitate. The resulting supernatant was then filtered using a syringe filter with a pore size of 0.22 μm.

g-CDs. 3,4,9,10-Tetranitroperylene was obtained by nitration of perylene at 80 °C for 12 h, with subsequent collection and drying of the precipitate at 60 °C. 25 mg of the prepared 3,4,9,10-tetranitroperylene powder was mixed with 15 mL of 0.2 M NaOH–ethanol mixture and then treated using a solvothermal procedure in a Teflon-lined stainless-steel autoclave at 200 °C for 12 h. The resulting suspension was purified *via* column chromatography (silica gel, pore size 60 Å) using methanol and ethanol as eluents.

r-CDs. Samples of r-CDs were obtained by conversion of g-CDs by adding dropwise a 1 M NaOH–ethanol solution until the emission color of the solution turned from green to red.

Structural characterization of b-CDs, g-CDs, and r-CDs

TEM images were obtained using a JEM 2010 microscope (Jeol). FTIR spectra were recorded on a NicoletiS5 FTIR spectrometer (Thermo Fisher Scientific) using the Smart Orbit ZnSe ATR crystal setup. XPS measurements were performed using a PHI VersaProbe II XPS spectrometer (Physical Electronics) equipped with an Al Kα source (15 kV, 50 W) and the results were analyzed by using Multipak (UIvac-PHI, Inc.) software. The spectral analysis included Shirley background subtraction and peak deconvolution using mixed Gaussian–Lorentzian functions. Raman spectra were recorded on a DXR Raman microscope (Thermo Fisher Scientific) using the 780 nm excitation line of a diode laser.

Fabrication of thin-film CD–polymer LSCs

b-CD LSC. A 12% PVA solution in water was prepared by stirring PVA in water at 95 °C for 5 h and further cooling to room temperature. 12.5 μL of the synthesized b-CDs (20 mg mL^{-1}) was mixed with 2 mL of 12% PVA solution in water to form a CD–polymer mixture with a b-CD concentration of 0.12 mg mL^{-1}, and the mixture was stirred overnight to obtain a homogeneous polymer slurry, and degassed in an ultrasonic bath for 5 min. A highly uniform b-CDs@PVA film on a glass substrate was prepared by drop-casting. After drying at 40 °C for 10 h, the thickness of the resulting film was 50 μm.

g-CD LSC. 11.5 mL of the g-CD–ethanol dispersion with a concentration of 2.9 mg mL^{-1} was mixed with PVP powder to form 500 mg mL^{-1} CD–polymer solution. The same procedures of stirring and degassing were performed to increase the quality of the polymer blend. The g-CDs@PVP solution was drop-cast onto a glass substrate, and the second glass with a gasket was attached on the top to form a sandwiched glass-CDs@polymer-glass structure. The polymerization was completed by drying the sample at 40 °C for 10 h. Then the gasket was removed, and the space was refilled with a CD–polymer solution. The thickness of the resulting film was 100 μm.

r-CD LSC. The CD–polymer mixture was prepared by mixing 9 mL of r-CDs dispersed in ethanol (3.1 mg mL^{-1}) with 4.5 g of PVP K30 powder. Sodium hydroxide was added dropwise to the obtained mixture until the emission color changed from green to red. 90 μL of 10% PEI (polyethylenimine) solution in ethanol was added to achieve better stability in an alkaline environment. The drop-casting method was used to create a highly uniform CDs/polymer film on a glass substrate (the film thickness was 80 μm).

Optical characterization

The UV-Vis absorption spectra of colloids and polymer films were recorded on spectrometers Specord S600 (Analytik Jena, Germany) and Specord Plus equipped with a solid-state holder (Analytik Jena, Germany), respectively. PL measurements were performed using an FLS980 fluorescence spectrometer (Edinburgh Instruments) equipped with a 450 W xenon arc lamp as the excitation source for steady-state experiments and with an EPL-375 picosecond pulsed diode laser (λ_{em} = 372 nm with a pulse width of 66.5 ps, a repetition rate of 10 MHz and an average power of 75 μW, also Edinburgh Instruments) for time-resolved measurements. The PL QY was determined by an absolute method using the same spectrometer with an attached integrating sphere (with its inner face coated with BENFLEC). Spectral correction curves were provided by Edinburgh Instruments. The accuracy of the integrating sphere apparatus was verified against a few reference dyes.

LSC performance characteristics

We used several characteristics to quantify the LSC performance. The optical quantum efficiencies (defined as the ratio between the number of photons emitted from the LSC edge and the total number of incident photons absorbed by it) at different excitation wavelengths (355 nm, 465 nm, and 550 nm) were determined for blue, green, and red LSCs using the same spectrometer and integrating sphere attached (see Fig. S7†). The PL QY of each LSC was obtained before ($PLQY_{total}$) and after ($PLQY_{surface}$) its edges were masked with a nontransparent black tape. The internal OQE was calculated as $\eta_{int} = PLQY_{total} - PLQY_{surface}$. Electro-optical measurements for the tandem LSC coupled to a commercial a-Si solar cell were performed with a LS0916 solar simulator (LOT-Quantum Design, Class AAA, 1000 W m^{-2}, continuous). The area of the solar cell was masked to fit the dimensions of the tandem LSC edge (8 × 0.8 cm) using a nontransparent black tape. *I–V* measurements (Keithley 2400 sourcemeter) were performed under a simulated AM 1.5G spectrum at one-sun intensity.

Results and discussion

Synthesis and characterization of CDs

Highly luminescent blue, green, and red emissive carbon dots (hereafter abbreviated as b-CDs, g-CDs, and r-CDs, respectively) were synthesized *via* a hydrothermal or solvothermal method (Fig. 1a) according to the previously published protocols with minor modifications.[44,45] Blue-emitting b-CDs were synthesized in water using citric acid and L-cysteine as precursors, whereas green- and red-emitting g-CDs and r-CDs were synthesized in ethanol using 3,4,9,10-tetranitroperylene as a single precursor (see the Experimental section for details). The size and morphology of the synthesized CDs were examined by transmission electron microscopy (TEM). Typical TEM images of b-CDs, g-CDs, and r-CDs are presented in Fig. 1b–d together with the corresponding size distribution histograms calculated from measurements of more than 100 observed CD particles of each type. The size of the synthesized carbon dots varies from 2 to 9 nm with average values of 6.3 ± 0.9 nm, 2.9 ± 0.5 nm, and 2.9 ± 0.7 nm for b-CDs, g-CDs, and r-CDs, respectively. The chemical structures of the CDs were characterized by X-ray photoelectron spectroscopy (XPS), Fourier-transform infrared spectroscopy (FTIR), and Raman spectroscopy. The obtained results are provided in the ESI (Fig. S2–S4†); they confirm that the CDs have a similar chemical composition and material structure to those reported in the previously published synthetic protocols.[44,45]

The optical properties of the blue-, green-, and red-emitting CDs were investigated in diluted colloidal solutions at room temperature (b-CDs were dispersed in water, and g-CDs and r-CDs in ethanol). PL excitation–emission maps for b-CDs, g-CDs, and r-CDs are presented in Fig. 2a–c, and the photographs of the emitting CDs under UV light (365 nm) are shown in the insets. All three CD samples show excitation-independent PL (*i.e.*, the position of the emission peak remains constant over a wide range of excitation wavelengths) suggesting that the PL in all three samples originates from uniform emissive states. UV-Vis absorption, the steady-state PL spectra, and the absolute PL QY data for the CDs are shown in Fig. 2d–f. The CDs exhibit two absorption bands, in particular a band located in the region of 200–250 nm (typically ascribed to the π–π* transition),[46] and a red-shifted absorption band. The presence of these two bands has been commonly ascribed in the literature to an interplay between the absorption of the graphitic core and the surface states.[47] The positions of the absorption peaks differ in the three CD samples, shifting from 344 ± 1 nm for b-CDs to 458 ± 1 nm and 538 ± 1 nm for g-CDs and r-CDs, respectively. The PL excitation spectra of the three CD samples extend over the entire visible range of the electromagnetic spectrum, covering the UV-blue range (b-CDs), and blue-green (g-CDs), and green-red (r-CDs) regions, which allows an efficient capture of solar radiation. The positions of PL excitation maxima for b-CDs, g-CDs, and r-CDs are at 352 ± 1 nm, 457 ± 1 nm, and 535 ± 1 nm with the corresponding full width at half-maxima (fwhm) of 53 ± 1 nm, 63 ± 1 nm, and 94 ± 1 nm, respectively. Emission spectra were obtained under the excitation of 355 nm, 460 nm, and 535 nm, and show the PL maxima centered at 420 ± 1 nm (b-CDs), 515 ± 1 nm (g-CDs), and 610 ± 1 nm (r-CDs) with the corresponding fwhm of 67 ± 1 nm, 76 ± 1 nm, and 66 ± 1 nm, respectively. The Stokes shifts calculated for the CDs as the difference between the peak position in the PLE (absorption) spectrum and the PL peak were 68 ± 1, 58 ± 1, and 75 ± 1 nm for b-CDs, g-CDs, and

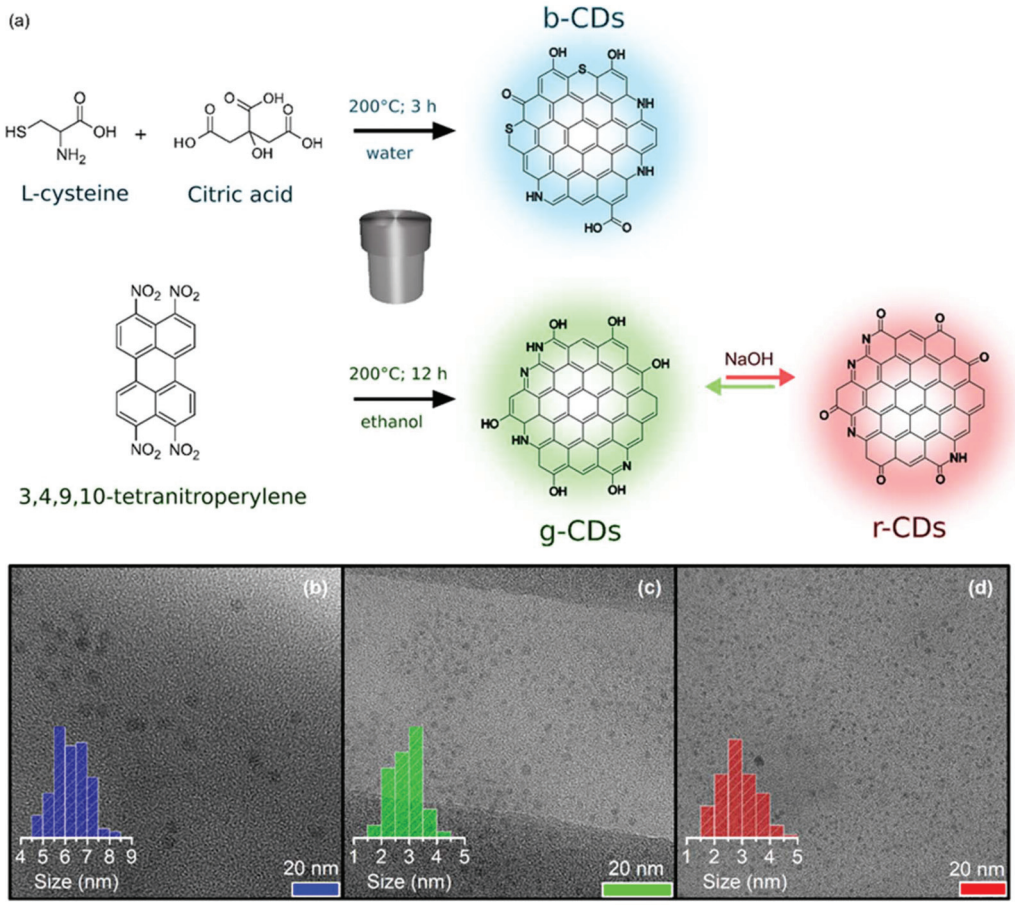

Fig. 1 The synthesis and morphology of b-CDs, g-CDs, and r-CDs. (a) Chemical reactions used for the synthesis of CDs. (b–d) TEM images of b-CDs (b), g-CDs (c), and r-CDs (d), with the corresponding size histograms provided in the insets.

r-CDs, respectively. The PL QY values for each sample (measured by an absolute method at the optimal excitation wavelength) were 63% for b-CDs, 78% for g-CDs, and 77% for r-CDs. Time-resolved PL decays for b-CDs, g-CDs, and r-CDs are shown in Fig. 2g–i; all of them could be well fitted by a single-exponential function, with extracted PL lifetimes of 9.8 ns for b-CDs, 3.9 ns for g-CDs, and 5.3 ns for r-CDs (see the Experimental section for details). The photostabilities of the CDs were tested under 1 mW cm^{-2} continuous monochromatic light illumination and no significant drop in the PL intensity was observed for b-CDs, g-CDs, and r-CDs for over 10 h (Fig. S5†).

Incorporation of CDs into transparent polymer matrices

In the next step, we focused on the incorporation of b-CDs, g-CDs, and r-CDs into suitable transparent polymer matrices. Three different polymers were identified as able to retain a high PL QY of the CDs during the encapsulation procedure, namely poly(vinyl alcohol) (PVA), polyvinylpyrrolidone (PVP), and a mixture of PVP and PEI, which were used in the fabrication of the following composite materials: b-CDs@PVA, g-CDs@PVP, and r-CDs@PVP + PEI. Their optical properties were investigated under identical conditions as in the case of colloidal solutions of CDs to achieve a fair comparison. The PL excitation–emission maps of the CDs@polymer composites deposited on quartz substrates are presented in Fig. S6a–c.† The PL emission of all three samples of CDs incorporated into polymers remains excitation independent. The position of the excitation maximum is slightly red-shifted compared to that of the ones in the colloidal solution and occurs at 355 ± 1 nm, 466 ± 1 nm, and 557 ± 1 nm with the corresponding fwhm of 50 ± 1 nm, 76 ± 1 nm, and 108 ± 1 nm for b-CDs, g-CDs, and r-CDs, respectively. The position of the absorption peaks is also red-shifted compared to the position of liquid phase measurements: 348 ± 1 nm and 468 ± 1 nm for b-CDs and g-CDs, respectively, and in the case of r-CDs the red shift in the absorption peak is accompanied by a shift in the absorption onset toward longer wavelengths (Fig. S6d–f†). PL emission spectra obtained under optimal excitation conditions show the PL maxima at 412 ± 1, 505 ± 1, and 612 ± 1 nm for b-CDs, g-CDs, and r-CDs, respectively. The absolute PL QY drops only slightly for all three samples of CDs embedded into polymers compared with those in the liquid phase, and are 52%, 71%, and 70% for b-CDs, g-CDs, and r-CDs, respectively. PL decays were measured and fit by suitable functions (two-exponential fit for b-CDs and g-CDs, and single-exponential fit

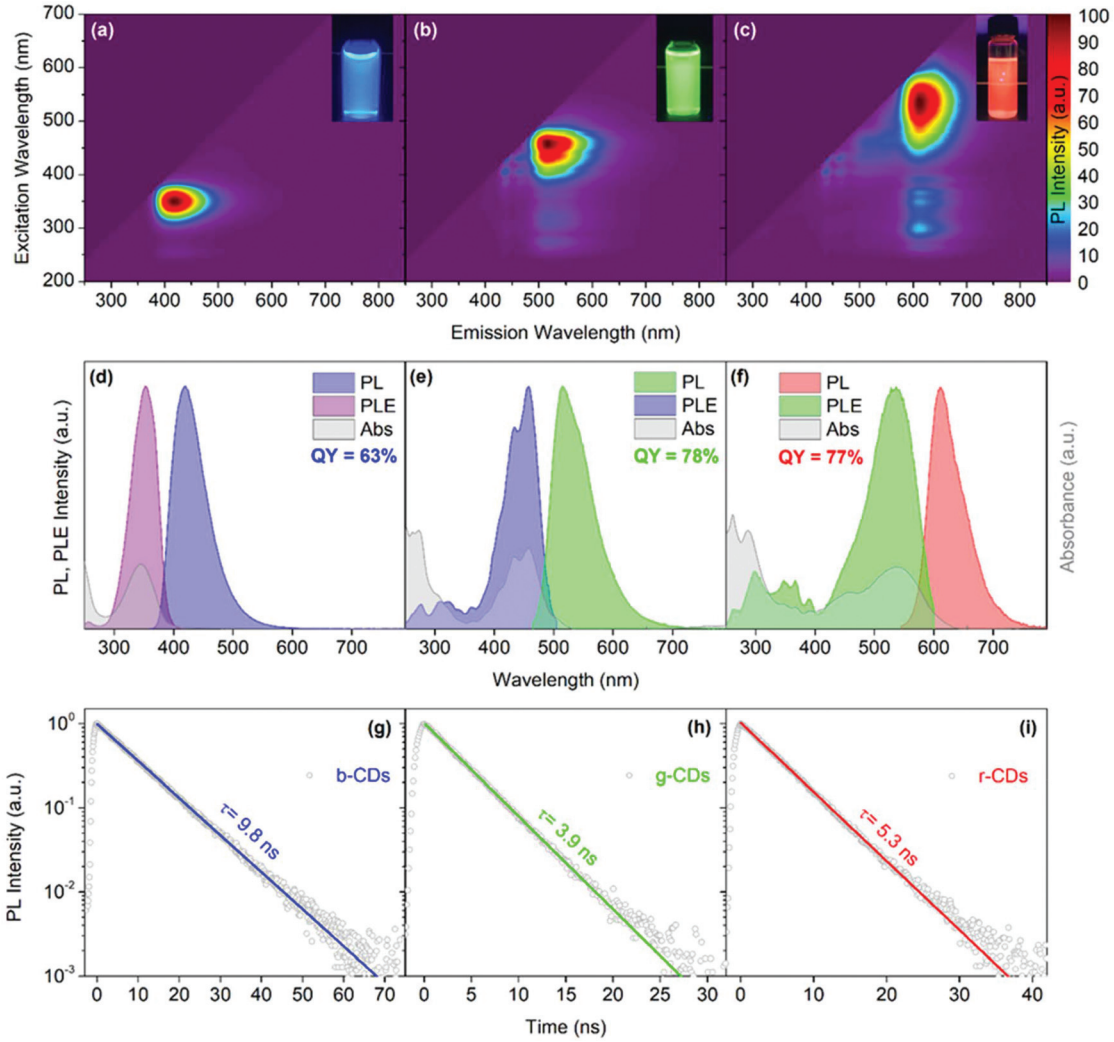

Fig. 2 The optical properties of b-CDs, g-CDs, and r-CDs. (a–c) Excitation–emission color maps. Insets: the photographs of the corresponding CD solution under UV light. (d–f) Absorption, PL excitation and emission spectra. (g–i) Time-resolved PL decays. Experimental data are represented by symbols, whereas solid lines are single-exponential fits (see the Experimental section for details).

for r-CDs) resulting in extracted average PL lifetimes of 7.4, 4.1, and 5.8 ns for b-CDs, g-CDs, and r-CDs, respectively (see Fig. S6g–i and Table S2†). As a result of the above studied optical properties, the application of CDs/polymer composites shows great promise for the use of CDs in the realization of highly efficient tandem LSCs.

Fabrication and characterization of individual CD-based LSCs

Three individual LSCs (abbreviated as b-LSC, g-LSC, and r-LSC according to the emission color of the corresponding CDs) were fabricated. It was reported that bulk polymerization of the monomer–fluorophore mixture resulting in all polymer LSC waveguides (PLMA[3] or PMMA[5]) leads to optical losses due to the scattering effects.[4,5,15] To reduce this effect, a layered LSC design was employed by deposition of the CD–polymer solution onto the 8 × 8 cm glass slabs using a drop-casting method. The photographs of the individual CD-based LSCs are shown in Fig. 3a–f. All three LSCs appear highly transparent under ambient light, with only slight tint of the respective colors (Fig. 3a–c). However, noticeable concentrated blue, green, and red light are clearly distinguishable at the edges of the glass slabs under low-intensity UV illumination (Fig. 3d–f). The PL excitation and emission spectra of the three individual LSCs are presented in Fig. 3g–i and they are also compared to the terrestrial AM1.5 spectrum of solar radiation. The excitation spectra of b-CDs, g-CDs, and r-CDs extend over the entire visible range, which allows efficient capture of solar radiation. Furthermore, absorptance (η_{abs}) values for all three layers at incident-light wavelengths were calculated according to eqn (1), resulting in 28.6, 23.1, and 17.9% for b-CD, g-CD, and r-CD LSCs, respectively.

$$\eta_{abs} = (1 - R)(1 - 10^{-OD}) \quad (1)$$

where R is the reflectance, and OD is the optical density at a specific wavelength.

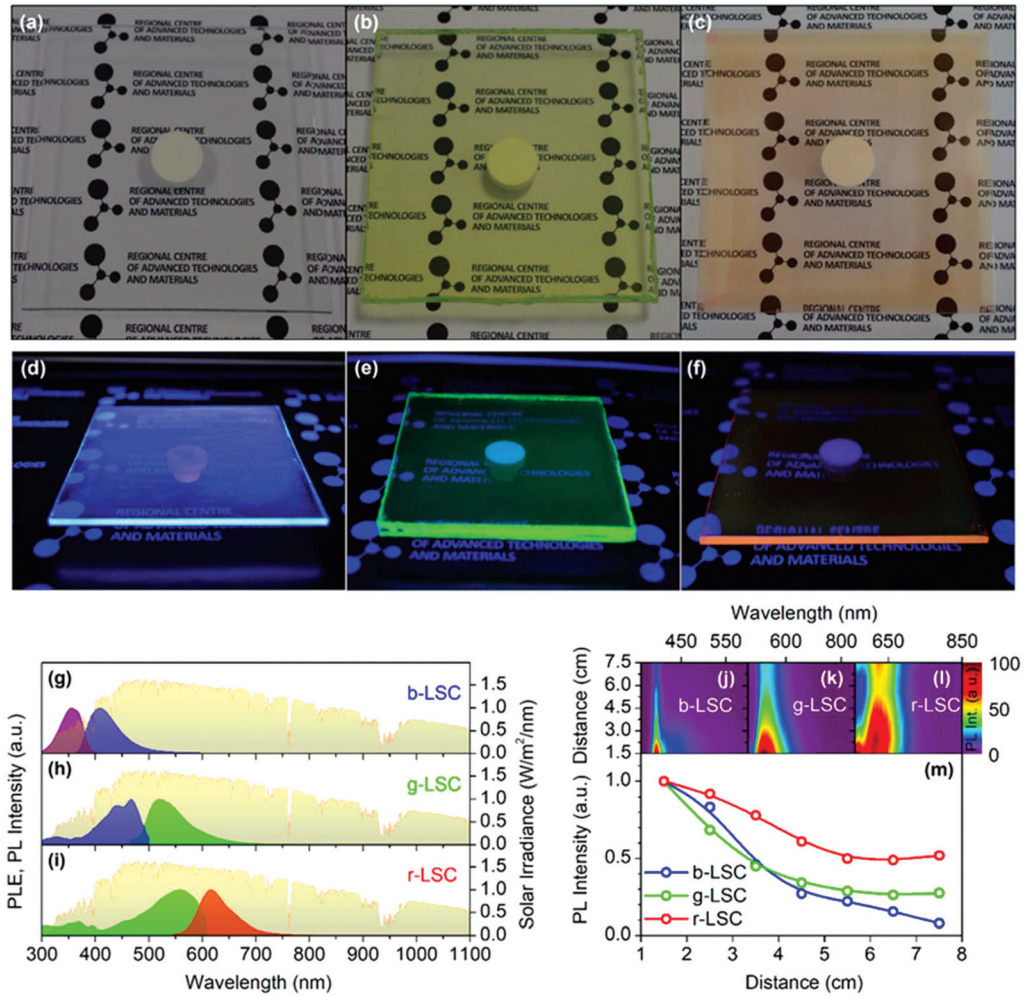

Fig. 3 Fabrication and characterization of the individual b-LSC, g-LSC, and r-LSC. (a–c) Photographs under ambient light and (d–f) under UV light. (g–i) The PL excitation and emission spectra of individual LSCs compared with the AM 1.5 solar spectrum (in yellow). (j–l) Color maps showing PL emission emerging from the LSC edge as a function of the distance between the excitation spot and the collection edge. (m) Spectrally integrated PL intensity from the LSC edges as a function of the propagation length.

To evaluate the optical losses for b-LSC, g-LSC, and r-LSC, we determined the PL QY values in an integrating sphere before ($PLQY_{total}$) and after ($PLQY_{surface}$) the edges of the LSCs were masked with a black nontransparent tape (Fig. S7†). Some decrease in the $PLQY_{total}$ values for large 8 × 8 cm devices was observed as compared to the values for the corresponding CDs in polymers deposited on a glass substrate due to reabsorption (the measured $PLQY_{total}$ values were 43.6, 50.1, and 50.1% for the b-LSC, g-LSC, and r-LSC, respectively).

The edge coupling efficiencies (η_{edge}) are 45.9, 66.5, and 73.7% for the b-LSC, g-LSC, and r-LSC, respectively, as obtained from eqn (2):

$$\eta_{edge} = \frac{PLQY_{total} - PLQY_{surface}}{PLQY_{total}} \quad (2)$$

where $PLQY_{total}$ is the PL QY of the whole LSC, and $PLQY_{surface}$ is the PL QY of the LSC with masked edges. The internal OQE (η_{int}) can be derived for each LSC using eqn (3):

$$\eta_{int} = \eta_{edge}\ PLQY_{total} = PLQY_{total} - PLQY_{surface} \quad (3)$$

The values of internal OQE were determined to be 20.0%, 33.3%, and 36.9% for the b-LSC, g-LSC, and r-LSC, respectively. The external OQE, η_{ext}, is defined as the ratio of the number of photons emitted from the LSC edges to the total number of incident photons (eqn (4)):

$$\eta_{ext} = \eta_{abs}\eta_{int} \quad (4)$$

The calculated external OQE values of the b-LSC, g-LSC, and r-LSC under monochromatic light illumination at the corresponding excitation maxima were 5.7%, 7.6%, and 6.6%, and 0.2%, 1.5%, and 1.0% taking the solar absorptance of each layer into account.

The optical losses of CD-based LSCs were also evaluated by obtaining the PL spectra from the edge of the LSC as a function of the optical path achieved by varying the distance between the excitation spot and the collection edge. Fig. 3j–l show the maps of the PL emission *vs.* the distance, whereas

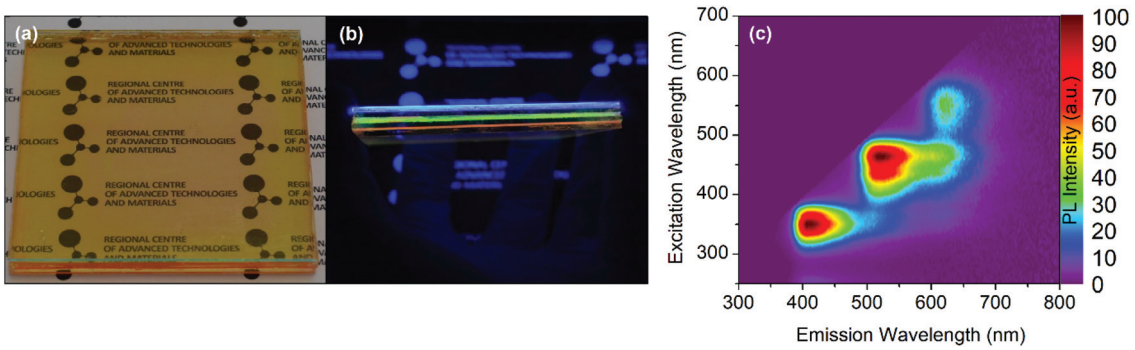

Fig. 4 Fabrication and characterization of the tandem LSC. (a) Photograph of the LSC under daylight, and (b) under weak UV illumination. (c) Excitation–emission color map (excited from the top of the device and the emission collected from the edge).

Fig. 3m demonstrates the dependence of the integrated PL emission as a function of the distance. In the case of the r-LSC, the PL intensity retains at least 50% of its initial value for the 7.5 cm optical path. The largest drop in the integrated PL (down to 8%) was observed for the b-LSC along the 7.5 cm optical path. The data derived from these measurements are in good agreement with the values of internal OQE.

Fabrication and characterization of a tandem CD-based LSC

A tandem LSC was fabricated by composing together all three constituent individual CD-based LSCs, namely b-LSC (top layer; $PLQY_{total}$ = 43.6% and $\eta_{s,abs}$ = 0.8%), g-LSC (middle layer; $PLQY_{total}$ = 50.1% and $\eta_{s,abs}$ = 4.4%), and r-LSC (bottom layer; $PLQY_{total}$ = 50.1% and $\eta_{s,abs}$ = 2.7%) in order to achieve high external OQE. An 8 × 8 cm prototype tandem LSC based solely on b-CDs, g-CDs, and r-CDs is shown in Fig. 4. The photographs of the tandem LSC device under ambient light and under UV illumination are shown in Fig. 4a and b, respectively. The tandem LSC appears transparent under ambient light, with orange color (Fig. 4a). Under low-intensity UV illumination, the concentrated blue, green, and red light is readily visible from the edge, coming from each constituent LSC (Fig. 4b). The extended coverage of the solar spectrum by the tandem LSC is demonstrated in Fig. 4c by its excitation–emission map. Three emission maxima are clearly visible on the map, each corresponding to the specific emission of the b-LSC, g-LSC, or r-LSC constituent.

To evaluate the potential of the tandem LSC for real-life applications, electro-optical measurements of an 8 × 8 cm tandem LSC coupled to a solar cell were performed under one-sun conditions (Fig. S8†). In this experiment, a-Si solar cell was edge-coupled to the tandem LSC with an index-matching polymer. Comparing the short-circuit currents of the solar cell alone, I_{LSC}, and the tandem LSC coupled to the solar cell, I_{PV} (Fig. S9†), the internal OQE can be derived as[2,4]

$$\eta_{int} = \frac{1}{G\eta_{s,abs}} \frac{I_{LSC}}{I_{PV}} \frac{Q_{total}}{Q_{PL}} \quad (5)$$

where G is the geometric factor, defined as the ratio between the area of the surface of LSC and the area of the edges (G = $A_{surface}/A_{edges}$), $\eta_{s,abs}$ is the solar absorptance of the LSC, I_{LSC} is the measured photocurrent of the standalone solar cell, I_{PV} is the photocurrent of the tandem-LSC coupled to the solar cell, and Q_{total} and Q_{PL} are the average external quantum efficiency (EQE) values of the solar cell over the total solar spectrum and around the PL peaks of CDs, respectively (Fig. S9†). The internal OQE of the 8 × 8 cm tandem LSC, calculated according to eqn (5), is 23.6%. This value is almost six-fold higher than that reported for the 10 × 10 cm CD-LSC.[26] The external OQE of the tandem LSC can be calculated as

$$\eta_{ext} = \eta_{s,abs}\eta_{int} \quad (6)$$

where $\eta_{s,abs}$ is the solar absorptance of the tandem LSC, and η_{int} is the internal OQE. The external OQE of the tandem CD-based LSC is 2.3%, which shows more than 50% enhancement compared with the highest external OQE obtained for the single CD-based LSC (g-LSC, 1.5%). Furthermore, this value is higher than that reported for the best-performing large area CD-based devices[26,31] and comparable with the latest results reported for hybrid CD-based tandem structures.[41,42] An overview of the literature results for LSCs based on semiconductor quantum dots, perovskite nanocrystals, and CDs can be found in Table S3 in the ESI.†

Conclusions

In summary, we have presented the first example of a large area (64 cm^2) thin-film tandem LSC that is based exclusively on environmentally friendly blue-, green-, and red-emitting CDs encapsulated in polymer matrices. The fabricated device exhibits an external OQE of 2.3% (corresponding to an internal OQE of 23.6%) combined with a high degree of transparency across the visible spectrum (83.4% transmittance). The fabrication process of these LSCs is cheap, environmentally friendly, and scalable, which makes them useful alternatives to classical semiconductor and perovskite quantum dot LSCs.

Conflicts of interest

There are no conflicts to declare.

Acknowledgements

The authors acknowledge the support from the Ministry of Education, Youth and Sports of the Czech Republic (LO1305 and CZ.1.05/2.1.00/19.0377) and the assistance provided by the Research Infrastructure NanoEnviCz, supported by the Ministry of Education, Youth and Sports of the Czech Republic under the Project No. LM2015073. The authors also acknowledge the support from the Operational Programme Research, Development and Education – Project No. CZ.02.1.01/0.0/0.0/15_003/0000416 of the Ministry of Education, Youth and Sports of the Czech Republic. L. Zdražil acknowledges the support from the Student Project IGA_PrF_2019_031 of Palacký University Olomouc. The authors gratefully thank K. Štymplová, J. Stráská, and J. Havláková for their expert assistance with material characterization.

References

1 M. G. Debije and P. P. C. Verbunt, *Adv. Energy Mater.*, 2012, **2**, 12–35.
2 M. Wei, F. P. G. de Arquer, G. Walters, Z. Yang, L. N. Quan, Y. Kim, R. Sabatini, R. Quintero-Bermudez, L. Gao, J. Z. Fan, F. Fan, A. Gold-Parker, M. F. Toney and E. H. Sargent, *Nat. Energy*, 2019, **4**, 197–205.
3 F. Meinardi, H. McDaniel, F. Carulli, A. Colombo, K. A. Velizhanin, N. S. Makarov, R. Simonutti, V. I. Klimov and S. Brovelli, *Nat. Nanotechnol.*, 2015, **10**, 878–885.
4 H. Li, K. Wu, J. Lim, H.-J. Song and V. I. Klimov, *Nat. Energy*, 2016, **1**, 16157.
5 F. Meinardi, A. Colombo, K. A. Velizhanin, R. Simonutti, M. Lorenzon, L. Beverina, R. Viswanatha, V. I. Klimov and S. Brovelli, *Nat. Photonics*, 2014, **8**, 392–399.
6 F. Meinardi, S. Ehrenberg, L. Dhamo, F. Carulli, M. Mauri, F. Bruni, R. Simonutti, U. Kortshagen and S. Brovelli, *Nat. Photonics*, 2017, **11**, 177–185.
7 F. Meinardi, F. Bruni and S. Brovelli, *Nat. Rev. Mater.*, 2017, **2**, 17072.
8 K. Wu, H. Li and V. I. Klimov, *Nat. Photonics*, 2018, **12**, 105–110.
9 M. J. Currie, J. K. Mapel, T. D. Heidel, S. Goffri and M. A. Baldo, *Science*, 2008, **321**, 226–228.
10 M. Rafiee, S. Chandra, H. Ahmed and S. J. McCormack, *Opt. Mater.*, 2019, **91**, 212–227.
11 S. Sadeghi, R. Melikov, H. B. Jalali, O. Karatum, S. B. Srivastava, D. Conkar, E. N. Firat-Karalar and S. Nizamoglu, *ACS Appl. Mater. Interfaces*, 2019, **11**, 8710–8716.
12 F. Meinardi, Q. A. Akkerman, F. Bruni, S. Park, M. Mauri, Z. Dang, L. Manna and S. Brovelli, *ACS Energy Lett.*, 2017, **2**, 2368–2377.
13 X. Luo, T. Ding, X. Liu, Y. Liu and K. Wu, *Nano Lett.*, 2019, **19**, 338–341.
14 H. Zhao, Y. Zhou, D. Benetti, D. Ma and F. Rosei, *Nano Energy*, 2017, **37**, 214–223.
15 V. I. Klimov, T. A. Baker, J. Lim, K. A. Velizhanin and H. McDaniel, *ACS Photonics*, 2016, **3**, 1138–1148.
16 C. S. Erickson, L. R. Bradshaw, S. McDowall, J. D. Gilbertson, D. R. Gamelin and D. L. Patrick, *ACS Nano*, 2014, **8**, 3461–3467.
17 Y. Zhou, D. Benetti, Z. Fan, H. Zhao, D. Ma, A. O. Govorov, A. Vomiero and F. Rosei, *Adv. Energy Mater.*, 2016, **6**, 1501913.
18 I. Coropceanu and M. G. Bawendi, *Nano Lett.*, 2014, **14**, 4097–4101.
19 G. Liu, R. Mazzaro, Y. Wang, H. Zhao and A. Vomiero, *Nano Energy*, 2019, **60**, 119–126.
20 L. R. Bradshaw, K. E. Knowles, S. McDowall and D. R. Gamelin, *Nano Lett.*, 2015, **15**, 1315–1323.
21 M. R. Bergren, N. S. Makarov, K. Ramasamy, A. Jackson, R. Guglielmetti and H. McDaniel, *ACS Energy Lett.*, 2018, **3**, 520–525.
22 C. Li, W. Chen, D. Wu, D. Quan, Z. Zhou, J. Hao, J. Qin, Y. Li, Z. He and K. Wang, *Sci. Rep.*, 2015, **5**, 17777.
23 M. Sharma, K. Gungor, A. Yeltik, M. Olutas, B. Guzelturk, Y. Kelestemur, T. Erdem, S. Delikanli, J. R. McBride and H. V. Demir, *Adv. Mater.*, 2017, **29**, 1–10.
24 N. D. Bronstein, L. Li, L. Xu, Y. Yao, V. E. Ferry, A. P. Alivisatos and R. G. Nuzzo, *ACS Nano*, 2014, **8**, 44–53.
25 Y. Li, P. Miao, W. Zhou, X. Gong and X. Zhao, *J. Mater. Chem. A*, 2017, **5**, 21452–21459.
26 Y. Zhou, D. Benetti, X. Tong, L. Jin, Z. M. Wang, D. Ma, H. Zhao and F. Rosei, *Nano Energy*, 2018, **44**, 378–387.
27 M. J. Talite, H. Y. Huang, Y. H. Wu, P. G. Sena, K. B. Cai, T. N. Lin, J. L. Shen, W. C. Chou and C. T. Yuan, *ACS Appl. Mater. Interfaces*, 2018, **10**, 34184–34192.
28 Z. Wang, X. Zhao, Z. Guo, P. Miao and X. Gong, *Org. Electron.*, 2018, **62**, 284–289.
29 X. Gong, W. Ma, Y. Li, L. Zhong, W. Li and X. Zhao, *Org. Electron.*, 2018, **63**, 237–243.
30 F. Mateen, M. Ali, H. Oh and S.-K. Hong, *Sol. Energy*, 2019, **178**, 48–55.
31 H. Zhao, *J. Lumin.*, 2019, **211**, 150–156.
32 Z. Li, X. Zhao, C. Huang and X. Gong, *J. Mater. Chem. C*, 2019, **7**, 12373–12387.
33 P. Devi, S. Saini and K. H. Kim, *Biosens. Bioelectron.*, 2019, **141**, 111158.
34 X. Bao, Y. Yuan, J. Chen, B. Zhang, D. Li, D. Zhou, P. Jing, G. Xu, Y. Wang, K. Holá, D. Shen, C. Wu, L. Song, C. Liu, R. Zbořil and S. Qu, *Light: Sci. Appl.*, 2018, **7**, 91.
35 T. Malina, K. Poláková, J. Skopalík, V. Milotová, K. Holá, M. Havrdová, K. B. Tománková, V. Čmiel, L. Šefc and R. Zbořil, *Carbon*, 2019, **152**, 434–443.
36 S. Kalytchuk, K. Poláková, Y. Wang, J. P. Froning, K. Cepe, A. L. Rogach and R. Zbořil, *ACS Nano*, 2017, **11**, 1432–1442.
37 J. B. Essner and G. A. Baker, *Environ. Sci.: Nano*, 2017, **4**, 1216–1263.
38 M. Semeniuk, Z. Yi, V. Poursorkhabi, J. Tjong, S. Jaffer, Z. H. Lu and M. Sain, *ACS Nano*, 2019, **13**, 6224–6255.
39 S. Kalytchuk, Y. Wang, K. Poláková and R. Zbořil, *ACS Appl. Mater. Interfaces*, 2018, **10**, 29902–29908.

40 F. Yuan, Z. Xi, X. Shi, Y. Li, X. Li, Z. Wang, L. Fan and S. Yang, *Adv. Opt. Mater.*, 2019, **7**, 1801202.
41 H. Zhao, D. Benetti, X. Tong, H. Zhang, Y. Zhou, G. Liu, D. Ma, S. Sun, Z. M. Wang, Y. Wang and F. Rosei, *Nano Energy*, 2018, **50**, 756–765.
42 W. Ma, W. Li, R. Liu, M. Cao, X. Zhao and X. Gong, *Chem. Commun.*, 2019, **55**, 7486–7489.
43 F. Mateen, M. Ali, S. Youn, S. Hoon and M. Jae, *Sol. Energy*, 2019, **190**, 488–494.
44 Y. Dong, H. Pang, H. B. Yang, C. Guo, J. Shao, Y. Chi, C. M. Li and T. Yu, *Angew. Chem., Int. Ed.*, 2013, **52**, 7800–7804.
45 B. Yuan, S. Guan, X. Sun, X. Li, H. Zeng, Z. Xie, P. Chen and S. Zhou, *ACS Appl. Mater. Interfaces*, 2018, **10**, 16005–16014.
46 S. Zhu, Y. Song, X. Zhao, J. Shao, J. Zhang and B. Yang, *Nano Res.*, 2015, **8**, 355–381.
47 Y. Xiong, J. Schneider, E. V. Ushakova and A. L. Rogach, *Nano Today*, 2018, **23**, 124–139.